ADVANCED FUNCTIONAL MATERIALS
www.afm-journal.de

Identifying the Signatures of Intermolecular Interactions in Blends of PM6 with Y6 and N4 Using Absorption Spectroscopy

*Daniel Kroh, Fabian Eller, Konstantin Schötz, Stefan Wedler, Lorena Perdigón-Toro, Guillaume Freychet, Qingya Wei, Maximilian Dörr, David Jones, Yingping Zou, Eva M. Herzig, Dieter Neher, and Anna Köhler**

In organic solar cells, the resulting device efficiency depends strongly on the local morphology and intermolecular interactions of the blend film. Optical spectroscopy was used to identify the spectral signatures of interacting chromophores in blend films of the donor polymer PM6 with two state-of-the-art nonfullerene acceptors, Y6 and N4, which differ merely in the branching point of the side chain. From temperature-dependent absorption and luminescence spectroscopy in solution, it is inferred that both acceptor materials form two types of aggregates that differ in their interaction energy. Y6 forms an aggregate with a predominant J-type character in solution, while for N4 molecules the interaction is predominantly in a H-like manner in solution and freshly spin-cast film, yet the molecules reorient with respect to each other with time or thermal annealing to adopt a more J-type interaction. The different aggregation behavior of the acceptor materials is also reflected in the blend films and accounts for the different solar cell efficiencies reported with the two blends.

1. Introduction

The efficiency of organic solar cells (OSCs) has remarkably improved within the last years to power conversion efficiencies surpassing 19% for single layer bulk-heterojunctions,[1–13] and beyond 20% for tandem cells.[14] This mainly results from the recent developments of nonfullerene acceptors (NFAs).[15] The NFAs adjustability in energy levels, electronic structure, and harvesting long-wavelength absorption allowed for significant advances of the solar cell efficiency over that obtained in fullerene-based acceptor devices.[15–19] This approach proved particularly successful when the so-called Y series acceptors, based on a general A–DA'D–A structure (A = acceptor moiety, D = donor moiety) and absorbing from 1.4 eV onward,

D. Kroh, K. Schötz, S. Wedler, M. Dörr, A. Köhler
Soft Matter Optoelectronics
Experimentalphysik II
University of Bayreuth
95440 Bayreuth, Germany
E-mail: anna.koehler@uni-bayreuth.de

F. Eller, E. M. Herzig
Dynamik und Strukturbildung-Herzig Group
Physikalisches Institut
Universität Bayreuth
Universitätsstr. 30, 95447 Bayreuth, Germany

L. Perdigón-Toro, D. Neher
Soft Matter Physics and Optoelectronics
Institute of Physics and Astronomy
University of Potsdam
Karl-Liebknecht-Str. 24-25, 14476 Potsdam-Golm, Germany

The ORCID identification number(s) for the author(s) of this article can be found under https://doi.org/10.1002/adfm.202205711.

DOI: 10.1002/adfm.202205711

G. Freychet
NSLS-II
Brookhaven National Laboratory
Upton, NY 11973, USA

Q. Wei, Y. Zou
College of Chemistry and Chemical Engineering
Central South University
Chansha 410083, P. R. China

D. Jones
School of Chemistry
Bio21 Institute
The University of Melbourne
30 Flemington Road, Parkville, VIC 3010, Australia

A. Köhler
Bayreuth Institute of Macromolecular Research (BIMF) and Bavarian Polymer Institute (BPI)
University of Bayreuth
95447 Bayreuth, Germany

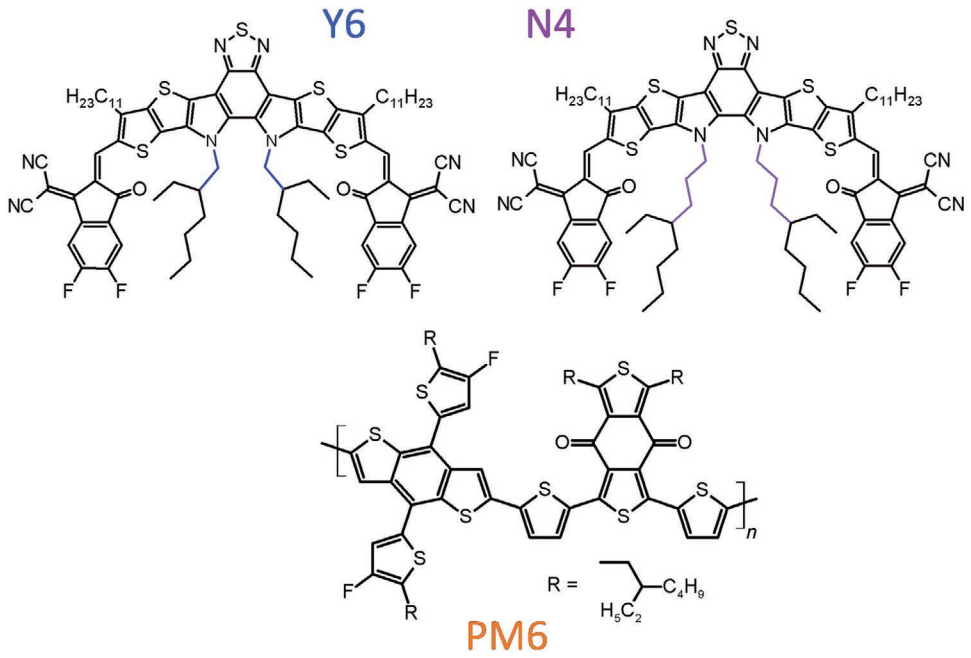

Figure 1. Chemical structures of Y6, N4, and PM6.

are combined with the polymer PM6 or related polymers (**Figure 1**).[2–3,20–23] PM6 has a general D–π–A structure with an optical gap around 1.8 eV.

The outstanding performance of these Y-type acceptor materials especially blended with PM6 prompted many groups to dedicate significant effort to understanding the reason behind this. The observed dependence of the device performance on the processing conditions and blend composition suggested a strong role of the molecular arrangements and order in the blend film.[24–27] This insight was further supported by the observation that side-chain modifications have a great impact on device performance. Side-chain modifications are well-known to alter the aggregation behavior and long-range order.[23,25–26,28–40]

It is well-known that the performance of OSCs does not only depend on the material itself, but rather on the arrangement and orientation of individual molecules with respect to neighboring molecules. It is the local morphology and the resulting intermolecular interactions that control the energy levels as well as optical and electronic properties of the material, including the efficiency of exciton dissociation and charge extraction in a device.[41–43] In consequence, the morphology of films with Y-type acceptors has been extensively studied by X-ray scattering. In single crystals, Y6 was found to form a "honeycomb" superstructure. Building blocks of this complex structure were identified in neat films of Y6 and in blend films made with Y6 and PM6. Molecular dynamics (MD) simulations and density functional theory (DFT) calculations allowed pinpointing dimer configurations that can make up these building blocks.[7,44]

We complement these investigations on Y-type acceptors by identifying the associated intermolecular interactions using optical spectroscopy. This provides information about both, noninteracting and interacting chromophores not only in highly ordered but also in amorphous phases. Our aim is to elucidate the presence and nature of such interactions in blend films of PM6 with two different Y-type acceptors. This requires first of all a clear identification of the optical signatures of intermolecular interactions in the neat materials. We therefore choose Y6 and N4 as electron acceptor materials (see Figure 1), which merely differ in the position of the branching point of the alkyl sidechains in the bay area of the molecule (2nd postion branching of the alkyl side-chains for Y6, 4th position branching for N4).

It has been previously observed that both materials show differences in their long-range order, and thus, we expect concomitant differences in their aggregation behavior and intermolecular interactions that will help to understand the role of the backbone and sidechains.[26,45] We are ultimately interested in blend films of PM6:Y6 and PM6:N4, which have previously been used by some of us to study the role of structural and energetic disorder on free charge recombination and open circuit voltage (V_{OC}).[25] For this, we will first identify the signatures of intermolecular interactions that show in solutions upon cooling, which is a well-established approach.[46–52] Cooling down the solution decreases the quality of the solvent. This induces interactions between the backbones of the sample molecules so that dimers or aggregates form. These interactions result in different absorption and photoluminescence spectra, which allows their identification and provides insight into the nature of the interactions.[53–54] The spectral signatures of intermolecular interactions in solution will then be used to recognize interacting chromophores in the spectra of neat film of Y6, N4, and PM6, and subsequently in blend films of PM6:Y6 and PM6:N4, which are more complex as the spectra of the components superimpose.

For each of the acceptors, we assign the spectral signatures from two different types of interacting chromophores, one with a larger interaction energy and one with a smaller one, while

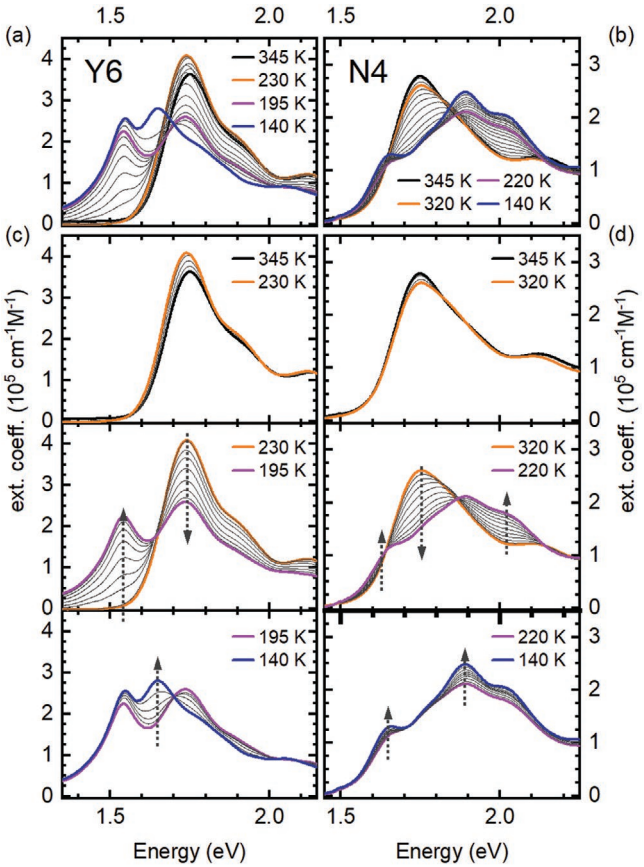

Figure 2. Absorption spectra of a) **Y6** (left) and b) **N4** (right) in MeTHF at a concentration of 0.15 mg mL^{-1} for different temperatures upon cooling from 345 to 140 K. Spectra taken at characteristic temperatures are drawn with colored solid lines and given in the legend. c,d) Spectra separated in three characteristic temperature ranges, respectively. Arrows indicate spectral changes in each temperature range.

there is only one type of interacting chromophores in the donor polymers PM6.

2. Results

2.1. Y6 and N4 in Solution

Figure 2 shows the absorption of Y6 and N4 in 2-Methyltetrahydrofuran (MeTHF) solution upon cooling from 345 to 140 K. A comparison of the full spectral evolution is shown in Figure 2a,b. Based on the spectral evolution of the absorption spectra upon cooling, we can group the spectra into three temperature ranges. These are displayed separately for clarity in Figure 2c,d. The corresponding emission spectra are shown in Figures S1 and S2 (Supporting Information). For Y6, the first characteristic temperature range is between 345 and 230 K (Figure 2b). At 345 K, the absorption spectrum has a peak centered at 1.75 eV and a shoulder at 2.90 eV. The linewidth, corresponding to a Gaussian linewidth with σ = 72 meV, is characteristic for noninteracting molecules with a distribution of conformations in solution. Upon cooling, the first absorption band increases slightly in intensity and shifts to lower energies by 10 meV. This behavior is indicative of an increase in conjugation due to a more planarized molecular backbone.[46–49,51–52] An additional analysis of the emission spectra and decay times (see Figures S1–S3, Supporting Information) confirms that the electronic interactions between the molecules do not change down to 230 K.

The second characteristic temperature range is between 230 and 195 K. In this range, a new spectral feature in absorption appears at 1.54 eV. Concomitantly, the absorption band at 1.75 eV decreases in intensity, resulting in an isosbestic point at 1.64 eV. The appearance of an additional absorption feature, accompanied by an isosbestic point, indicates the transformation of one phase into another. This can be considered as a disorder–order transition with an onset temperature of T_{onset} = 230 K, which is the first temperature upon cooling where signatures of aggregates can be observed.[47–48,51–52] Evidently, individual solvated Y6 molecules start to interact electronically, thus forming physical aggregates. We further observe a rise in the baseline, which is characteristic for light scattering from small particles.

The lowest investigated temperature range between 195 and 140 K is shown on the bottom panel of Figure 2c. Below 190 K, there is another phase transition as evidenced by the emergence of a new peak at 1.65 eV, accompanied by a new isosbestic point at 1.70 eV. The observation of a second isosbestic point with T_{onset} = 195 K hints to the formation of a second type of aggregate. This is unusual for organic semiconducting materials in solution and has only been reported in a few cases.[49,55]This phenomenon will be discussed further after analyzing the spectra in more detail.

The temperature-dependent spectral changes of N4 upon cooling from 345 to 140 K, i.e., the derivative that differs from Y6 merely in the branching point of the side-chains, are displayed in Figure 2b,d. Despite this subtle change, a different evolution with temperature compared to Y6 is readily obvious when comparing Figure 2a,b. For N4, the first characteristic temperature range is from 345 to 320 K. At 345 K, N4 still shows a similar absorption spectrum to Y6 with a maximum in absorption at 1.75 eV and a shoulder at 1.90 eV. However, in contrast to Y6, the intensity of the absorption band at 1.75 eV does not increase upon cooling but rather decreases. Notably, in the second temperature range, from about 320 K downward, we observe the appearance of additional absorption features at 1.66, at 1.89, and at 2.02 eV, and with two isosbestic points at 1.64 and 1.87 eV. Evidently, there is a phase transition of N4 with an onset temperature at around T_{onset} = 320 K. In contrast to Y6, the new phase in N4 is not characterized merely by an obvious new peak at lower energy (1.66 eV), but also by an intense band at higher energy (1.89, 2.02 eV), which is a more unusual observation. We again take these features as indication for the presence of electronically interacting chromophores, such as physical aggregates. In the lowest investigated temperature range, when cooling below 220 K the new absorption features increase in intensity and become more structured, while the intensity of the original contribution at 1.75 eV remains constant. This suggests that the number of aggregates formed remains constant below 220 K, yet the molecules in the aggregates further optimize their geometry, e.g., by planarization.[47,49,56] In contrast to

Y6, we do not observe the separate appearance of a different type of aggregate below 220 K. Upon heating, the same spectral features are obtained than upon cooling, albeit with a small temperature hysteresis (Figure S4, Supporting Information). We also measured the spectra in chloroform solution for the temperature range from 330 K (close to the boiling point of CF) down to 215 K (close to the melting point of CF), and observe the same trends as detailed in Figure S5 (Supporting Information).

2.2. Spectral Analysis

The temperature-dependent absorption measurements suggest the formation of electronically interacting chromophores when the solubility of the molecule in solution is sufficiently poor. To identify the optical signatures of the interacting chromophores and to disentangle them from the spectra of the noninteracting chromophores, we use Kasha's dimer model as a simple yet sufficient approximation. This is illustrated for reference in **Figure 3**, though we note that the number of interacting chromophores may be larger than two.[57] As widely known, in this framework interactions between adjacent molecules lead to an energetic splitting of the excited state, with one energy level above and one below the energy of the excited state of the monomer (see Figure 3). In the case that the dispersion shift is negligible compared to the splitting of the energy levels, the latter are located symmetrically around the energy level of the excited state of the monomer.[57,58] Frequently, the molecules arrange so that all oscillator strength lies in the transitions to the lower or upper of the two levels, which is referred to as H- or J-type dimers (or aggregates, if more than two molecules are involved), and then consideration of only one level for the interacting chromophores is sufficient. The special curved geometry of the Y-type acceptor molecules however allows for various mutual interaction possibilities and arrangements.[7] We therefore explicitly consider both energy levels to model the absorption from one type of interacting chromophores.

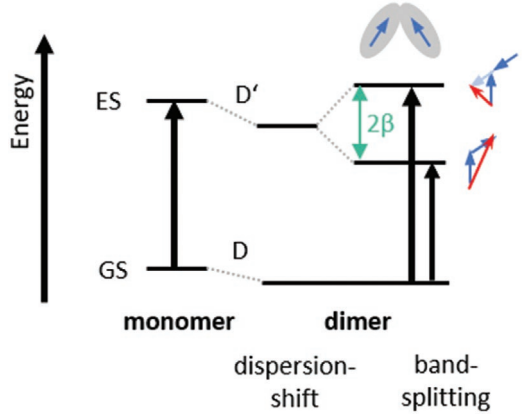

Figure 3. Oblique orientation of the dipoles of two molecules with the energy levels (GS: ground state, ES: excited state) for a monomer and the dimer, considering the dispersion shift $\Delta D = D–D'$ and the effect of the exchange energy β. The resulting transitions are displayed by the black arrows. The blue arrows indicate the transition dipoles of the corresponding molecules, the red arrows the total transition dipole moment.

Thus, to disentangle the different contributions to the absorption spectrum, we model the absorption spectra as a superposition of transitions, represented by Franck–Condon (FC) progressions. We first focus on the absorption spectra at a temperature just above the onset of the phase transition, where only noninteracting molecules prevail (i.e., at T = 230 K for Y6, at T = 320 K for N4). Based on Raman measurements of Y6,[59] we use a single effective vibrational mode of $\hbar\omega = 162$ meV for both materials, Y6 and N4. This is justified since the two molecules only differ in the branching point of the alkyl side chains. We use one FC progression for the $S_0 \rightarrow S_1$ transition with a 0-0 energy of 1.74 eV and a second FC progression with the same Gaussian linewidth yet with a different Huang–Rhys parameter for the $S_0 \rightarrow S_2$ transition at about 2.15 eV. For both progressions, the Huang–Rhys parameter was optimized to best match the experimental spectra. The fit parameters are detailed in Table S1 and Figure S6 (Supporting Information).

We next considered the absorption spectra for Y6 at 230 and at 195 K, where we observed the additional absorption from interacting chromophores. To account for transitions to the two possible levels of one type of interacting chromophores, we add two further progressions, on redshifted and one blueshifted relative to the progression of the noninteracting molecules (marked by solid and dashed lines, respectively, in **Figure 4**). Even though we do not know whether the interacting chromophores are exactly two or maybe more molecules, we shall henceforth refer to them as aggregates in the implicit understanding that the limiting case of a dimer is included in this term. We constrain the two progressions pertaining to the lower and upper level of the aggregate to have the same dominant intramolecular effective vibrational mode of $\hbar\omega = 162$ meV as the noninteracting chromophores, yet since the aggregate may experience a narrower effective disorder, we allow the linewidth to differ from the noninteracting molecule. We further impose a symmetric splitting around the 0-0 energy of the noninteracting molecule, after accounting for a dispersion shift ΔD. It turns out that a satisfactory fit to the experimental data cannot be obtained by considering only one type of aggregate, as detailed further in c.f. Figure S7 (Supporting Information). Rather, a second type of aggregate needs to be included with low intensity. The same modeling approach was used for N4.

Figure 4 shows the spectral decomposition of the absorption spectra in solution of Y6 and N4 at two temperatures, respectively. **Table 1** summarizes the Franck–Condon fit parameters for Y6 at 195 K and N4 at 220 K, i.e., 0-0 transition energy E_{00}, Gaussian linewidth parameter σ, Huang–Rhys parameter S_1, vibrational energy $\hbar\omega$. Values for 140 K and for the S_2 transition of the noninteracting chromophores can be found in the Supporting Information. We name the aggregate with the larger energetic splitting *aggregate I* (colored in red in Figure 4) and the one with smaller splitting *aggregate II* (colored in blue). The indices LE and HE refer to the lower and higher energy level for each aggregate.

There are several noteworthy features. Table 1 allows us to derive the values for the dispersion shift ΔD and the interaction energy β simply by rewriting the 0-0 transition energies to the aggregate as $E_{00} = E_M + \Delta D \pm \beta$. The resulting values are summarized in **Table 2**, along with an indication of the intensity of the 0-0 transitions relative to that of the amorphous phase at

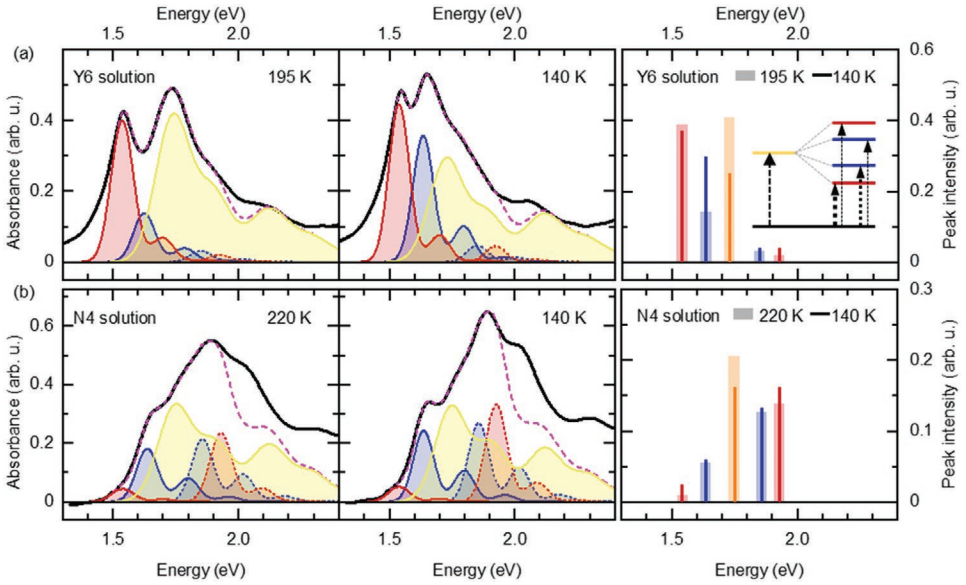

Figure 4. Spectral decomposition of the absorption spectra of a) Y6 and b) N4 in MeTHF solution at characteristic temperatures (195, 140 K for Y6 and 220, 140 K for N4) via a Franck–Condon Fit (detailed description in text). The disordered phase is colored in yellow, aggregate I in red and aggregate II in blue, each with their two progressions energetically below (solid line) and above (dashed line) the disordered phase. The global fit is displayed as pink dashed line. Additionally, we display the fractional intensity of each phase at 195/220 K as transparent bar and at 140 K as solid lines on the right side for both materials. A scheme of the underlying phenomenon of the energy level splitting is displayed in the top right graph.

195 K. The values for ΔD and β obtained for 140 K are almost identical except for the intensity of the transitions and can be found in the Supporting Information.

In summary, for Y6 we find that at 195 and at 140 K two different types of aggregates exist in the solution, in addition to the noninteracting chromophores. The absorption of aggregate I and aggregate II has some oscillator strength to both of the two split energy levels, yet the transition to the lower level dominates, akin to J-type aggregation. On the right side of Figure 4a, the associated intensities are displayed, normalized to sum up to one. The transparent bars show the intensities at 195 K, while the solid lines show the intensities at 140 K. At 195 K, the spectrum is dominated by comparable contributions from aggregate I and from noninteracting chromophores. Upon cooling to 140 K, the contribution from noninteracting chromophores reduces further and concomitantly that from aggregate II increases, while the amount of aggregate I remains constant. Thus, below 195 K, a disorder–order transition takes place resulting almost without exception in the formation of aggregate II. Evidently, aggregate I has the stronger interaction energy and forms more readily even at a higher temperature, while aggregate II has a lower interaction energy and forms with less ease. As we performed the 140 K measurements on the same solution after the 195 K measurements, we cannot unambiguously distinguish whether aggregation II necessarily requires lower temperatures, i.e., a poorer solvent quality, or whether more time might already be sufficient for its formation.

Figure 4b shows the spectral decomposition of N4 in solution at 220 and 140 K with the corresponding intensities of the different species shown on the right side. We identify transitions to aggregates at about the same energetic positions as

Table 1. The parameters for the FC-progressions used in Figure 4.

	Transition	E_{00} [eV]	σ [meV]	S_1	$\hbar\omega$ [meV]
Y6 in MeTHF 195 K	Noninteracting	1.74	69	0.43	162
	Agg. I, LE	1.54	44	0.15	162
	Agg. I, HE	1.92	44	0.15	162
	Agg. II, LE	1.62	44	0.26	162
	Agg. II, HE	1.85	44	0.26	162
N4 in MeTHF 220 K	Noninteracting	1.74	68	0.55	162
	Agg. I, LE	1.54	44	0.18	162
	Agg. I, HE	1.93	44	0.18	162
	Agg. II, LE	1.64	43	0.40	162
	Agg. II, HE	1.86	43	0.40	162

Table 2. Dispersion shift, interaction energy, and fractional intensity for the aggregates in Y6 and N4 in MeTHF. The fractional intensity is shown for the low energy phase (LE) and high energy phase (HE) of the aggregates, respectively.

	ΔD [meV]	β [meV]	Fractional intensity	
			LE	HE
Y6, Noninteracting 195 K	–	–	0.41	
Y6, Agg. I at 195 K	–15	195	0.39	0.02
Y6, Agg II at 195 K	–10	110	0.14	0.03
N4, Noninteracting 220 K			0.34	
N4, Agg. I at 220 K	–15	195	0.04	0.23
N4, Agg. II at 220 K	0	110	0.18	0.21

for Y6, and with similar interaction strength, yet with a clearly different intensity distribution. In contrast to Y6, at 220 K, the absorption of *aggregate I* (red) in N4 takes place mainly to the higher energy level, akin to a H-type aggregate, and the absorption to *aggregate II* (blue) takes place with almost equal intensity to both split energy levels.

Upon cooling down to 140 K, the distribution of oscillator strength remains nearly unchanged, except that the intensity of absorption from noninteracting chromophores reduces slightly relative to that from the aggregate. This very different distribution of oscillator strength in N4 compared to Y6 suggests that N4 forms dimers with similar interaction energy as Y6, yet with different relative orientations of the molecules. In simplified terms, one could associate the two aggregates in Y6 with a J-type character, and those in N4 with a more H-type character or oblique orientation of dipole moments. This assignment is consistent with the observed PL intensities (see the Supporting Information).

It is remarkable that this change in orientation of the interacting chromophores as well as the higher onset temperature of N4 is brought about merely by the change in the branching point of the side chain. In N4, the branching point is further away from the backbone than in Y6, reducing steric constraints for the mutual orientation of chromophore backbones and exposing the π-system. We speculate that this, first, increases the likelihood of π–π-stacking allowing for aggregation already at higher temperatures, and second permits a staggered backbone arrangement with partial overlap between donor and acceptor sites in N4, that may be precluded in Y6. The group of Brédas identified several dimer configurations by molecular dynamics simulations, either with more J-like or H-like character, which may correspond to the aggregate configurations observed with our spectroscopic analysis.[7,44] This will be further discussed below. The observation of several aggregate types is not surprising in Y6 since a complex honeycomb structure has been previously confirmed, which consists of different dimer configurations.[6–7,60]

2.3. Neat Y6 and N4 Films

Having identified the prevailing aggregates and their spectral characteristics in solution, the next step toward understanding the blend film composition is a spectral analysis of neat films for the acceptor materials, Y6 and N4. **Figure 5**a,b shows the absorption of Y6 and N4 films, spun from a solution of chloroform with 0.5% chloronaphtalene (CN) as-cast (ac, dotted lines) and after thermal annealing for 5 min at 90 °C (TA, blue and purple solid lines, respectively). These preparation conditions are well-known to achieve the best performances in solar cells made with blend films. For reference, the absorption in solution at 140 K is indicated as gray dotted line (sol.).

The first transition band of the neat, as-cast Y6 film has a dominant absorption peak at 1.55 eV with shoulders at 1.68 and 1.91 eV. Centered at 2.5 eV, a weak and structureless second transition band is evident. Annealing the neat Y6 film results in only small changes, where the low energy peak position slightly shifts to lower energies. Comparing the film spectra with the absorption in MeTHF solution at 140 K, it is evident that the observed peak at 1.55 eV and the shoulder at 1.68 eV of the films coincide with the energetic position of the peaks

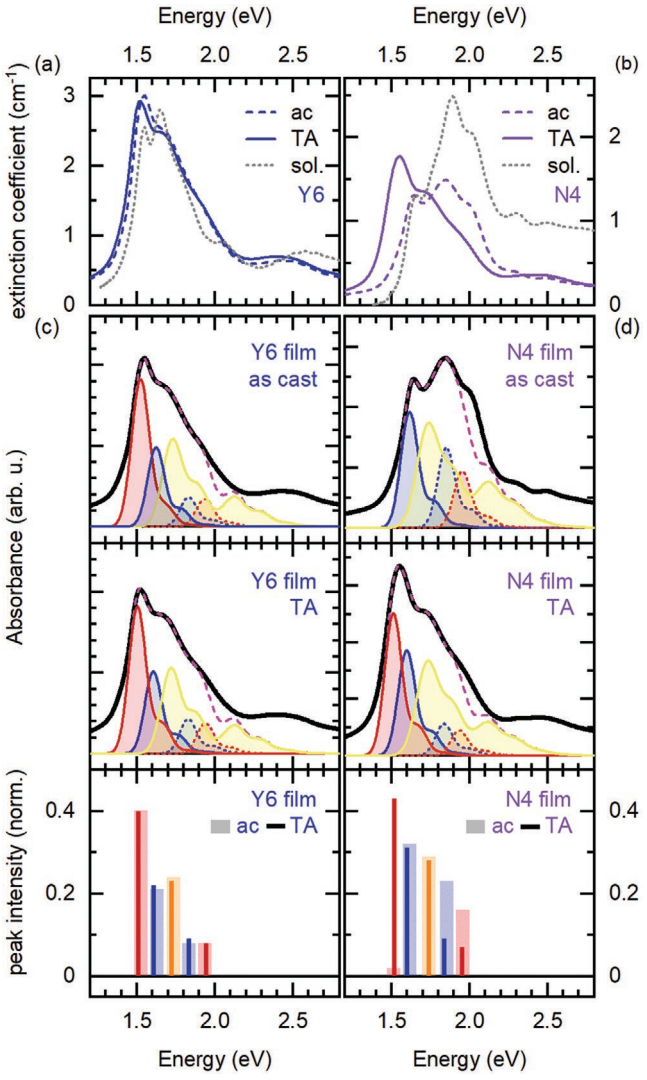

Figure 5. Absorption spectra of as-cast (dashed line) and thermally annealed (solid line) films of a) Y6 and b) N4. Additionally, the absorption in solution at 140 K is depicted (gray, dotted line), respectively. Spectral decomposition of the absorption spectra of the as-cast (top) and thermal annealed (middle) films of c) Y6 and d) N4 via a Franck–Condon Fit (detailed description in text). The disordered phase is colored in yellow, *aggregate I* in red and *aggregate II* in blue, each with their two progressions energetically below (solid line) and above (dashed line) the disordered phase. The global fit is displayed as pink dashed line. For a better comparison, we depict the peak intensity of each phase according to the spectral decomposition of the as-cast (transparent bar) and TA (solid line) film in one graph on the bottom.

of both aggregate types observed in solution, though the peak intensities differ slightly. For N4, the peak positions in the as-cast film also coincide with those in MeTHF at 140 K, yet the relative peak intensities differ strongly. Furthermore, and also in contrast to Y6, the absorption spectrum of the neat N4 film changes drastically in shape and position by thermal annealing, with a dominant lower energy peak emerging. As a result, the annealed N4 film appears similar to the spectrum of the Y6 film. Qualitatively the same spectral change is observed in N4 when, instead of annealing, the as-cast film is left to rest

Table 3. The parameters for the FC-progressions used in Figure 4.

	Phase[a)]	E_{00} [eV]	σ [meV]	S_1	$\hbar\omega$ [meV]
Y6 film as-cast	Noninteracting	1.73	64	0.42	162
	Agg. I, LE	1.52	57	0.13	162
	Agg. I, HE	1.93	57	0.13	162
	Agg. II, LE	1.62	55	0.20	162
	Agg. II, HE	1.83	55	0.20	162
N4 film as-cast	Noninteracting	1.73	70	0.48	162
	Agg. I, LE	1.51	55	0.18	162
	Agg. I, HE	1.95	55	0.18	162
	Agg. II, LE	1.61	55	0.20	162
	Agg. II, HE	1.85	55	0.20	162

[a)]The FC-parameters for the TA films are very similar to the as-cast films for both, Y6 and N4, and can be found in the Supporting Information.

Table 4. Dispersion shift and interaction energy for the aggregates in Y6 and N4 in film.

		ΔD [meV]	β [meV]	Fractional intensity[a)]	
				LE	HE
Y6, as cast	Noninteracting	–	–	0.24	
	Agg. I	−5	205	0.40	0.08
	Agg. II	−5	105	0.21	0.08
Y6, TA	Noninteracting	–	–	0.23	
	Agg. I	+5	220	0.40	0.08
	Agg. II	+10	115	0.22	0.09
N4, as-cast	Noninteracting			0.29	
	Agg. I	–	215	0.0	0.16
	Agg. II	−5	120	0.32	0.23
N4, TA	Noninteracting			0.28	
	Agg. I	−5	215	0.43	0.07
	Agg. II	−15	120	0.31	0.09

[a)]Intensities normalized so that intensities of all phases add up to 1 in the respective as-cast film.

and measured again after 3 months (see Figure S8, Supporting Information). We point out that the extinction coefficient of the annealed Y6 film is almost twice the value of the annealed N4 film. Thus, the difference in the absorption of Y6 and N4 in the film is manifested in two features, that is an overall lower intensity of the N4 absorption, which is not present in solution, and a significant change in shape and position after annealing.

Figure 5c,d shows the spectral decompositions of the neat films, as-cast and thermal annealed, using the same approach as for the spectra in solution. For Y6, we find aggregates with similar energetic positions, Huang–Rhys parameters, coupling strength and even relative intensities in the as-cast or TA films as in solution, as detailed in **Tables 3** and **4**. Only the linewidth of the aggregates in the film is increased from roughly σ = 44 meV to σ = 56 meV when going from solution to film. This testifies that during film formation with the given preparation conditions, Y6 forms the same aggregates as in solution upon cooling. For N4, we also find two types of aggregates, at approximately the same energetic positions as in solution and as in Y6, and with similar Huang–Rhys factors. Even coupling strength and the change in linewidth from solution to film are similar to Y6. The feature that causes the strikingly different absorption in N4 is the different distribution of oscillator strength. Comparing the as-cast film to the MeTHF solution, we see a lesser contribution of the higher aggregate levels, a stronger contribution of the lower level of aggregate II, and, most prominently, a nearly complete absence of the lower level of aggregate I. Upon annealing, this level acquires significant oscillator strength, while that of the upper aggregate levels reduces, so that the distribution of oscillator strength is now closer to the case in Y6. Evidently, annealing N4 causes a significant reorientation of molecules with respect to each other toward a geometry that supports more J-type aggregation.

In summary, upon film formation we observe the formation of aggregates with similar energy levels as in solution. However, we find an overall lower absorption strength in the N4 film compared to the Y6 film, and we observe the signature of a significant change in geometric orientation between individual molecules after annealing. After annealing, the very similar spectra of Y6 and N4 suggest a similar orientation between molecules.

These findings can be compared against results obtained from grazing-incidence wide-angle X-ray scattering (GIWAXS) measurements. **Figure 6**a shows the 2D maps of the scattering patterns of N4 and Y6 films on silicon, as-cast and after thermal annealing, respectively. Reference measurements on glass, confirming the analogous behavior of the examined materials on both substrate types, can be found in the Supporting Information. Both N4 films, as-cast and thermally annealed, show intensity at around 1.8 A^{-1} predominantly in horizontal (q_{xy}) direction. This is indicative for π–π stacking with an edge-on orientation to the substrate. In contrast, the Y6 film shows intensity at around 1.8 A^{-1} in vertical (q_z) direction, indicating a π–π stacking in face-on orientation consistent with previous publications.[2,6,25,61] This difference in backbone orientation between N4 and Y6 accounts for the higher absorption intensity of Y6. Since the transition dipole moment is in the plane of the molecules, more intense absorption is possible for the predominant face-on orientation of Y6 compared to the edge on orientation of N4. The scattering images show no changes in the fundamental orientation upon thermal annealing.

The nature of nanostructure of the aggregates, as obtained from the low q-values, also differs between Y6 and N4 films. The horizontal and vertical cuts at low q-values are shown in Figure 6b. For the Y6 as-cast film we observe multiple clearly defined peaks at 0.22, 0.34, and 0.44 A^{-1} in horizontal direction and at 0.52 and 0.62 A^{-1} in vertical direction. This suggests a sample containing a complex structure. Upon annealing, only the peak intensities slightly change, which can also arise from small differences of the film thickness. The as-cast N4 film, in contrast, shows only one peak in this q range at 0.32 A^{-1}

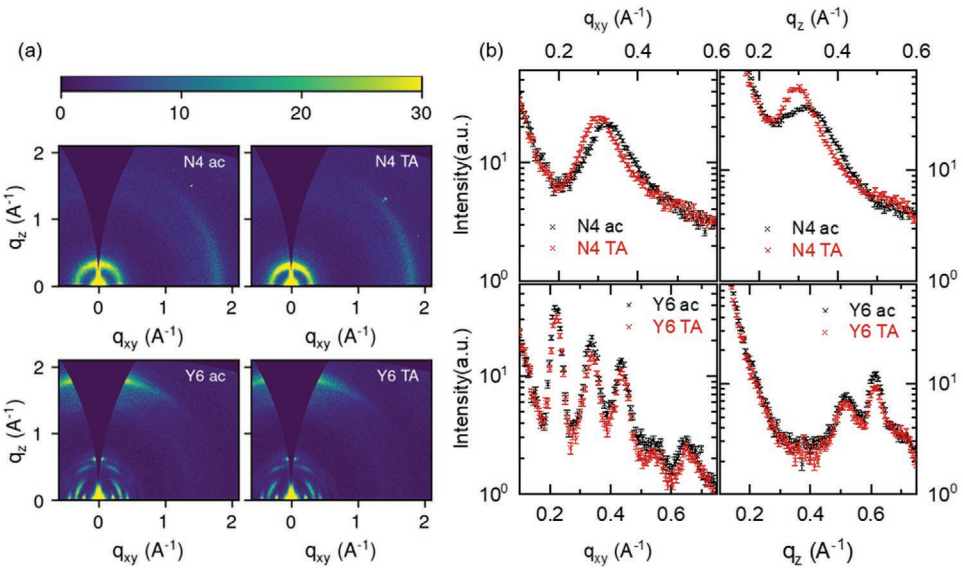

Figure 6. a) 2D-GIWAXS images of N4 (top) and Y6 (bottom) films, as-cast (left) and after thermal annealing (right) measured on Si substrates. b) Horizontal (left) and vertical (right) line cuts of the as-cast and thermal annealed films of N4 (top) and Y6 (bottom).

in horizontal and vertical direction. Hence, there is less pronounced order in as-cast films of N4 compared to Y6 which shows a clear superstructure beyond single molecules. Upon thermal annealing, we observe a significant change in the scattering pattern of N4. The main peak shifts to smaller q-values with a peak at 0.30 A^{-1} in both directions. This shift is accompanied by an intensity gain in vertical direction, indicating an increase in the preferred orientation. The change in peak position and intensity suggests a significant adjustment of the nanostructure including an increase of the lattice parameter.

Evidently, the shift to smaller q_z values upon annealing N4 correlates with the redistribution of oscillator strength to the lower aggregate levels, and thus a reorientation of the transition dipole moments. However, as displayed in Figure 5, after annealing, the films of N4 and Y6 are characterized by very similar intermolecular electronic interaction, that is two kinds of predominantly J-like aggregates, in addition to a disordered phase, while they still differ significantly in their nanostructure, as demonstrated by the strikingly different GIWAXS data (Figure 6b). The difference in the formed nanostructures in N4 is even more striking when considering that N4 has aggregates in solution already at room temperature at the start of film formation, so that extended structures could potentially form during the entire drying process. But even in the dried film the structural order is not as well defined for N4 as for Y6 as observed by scattering. This method includes the investigation of structural order beyond individual molecules in contrast to spectroscopy. The Y6 nanostructure shows smaller peak width in the scattering data due to larger coherence lengths which can be translated to a molecular ordering with a range of almost 20 nm, while it is only about 7 nm for N4. This well-defined honeycomb nanostructure occurs during film formation, although Y6 at room temperature does not yet show signatures of aggregation in solution. We speculate that on the one hand, the longer side chains of N4 allow for an easier aggregation of individual molecules, however, on the other hand these longer side chains also induce steric hindrance such that larger complex nanostructures cannot be formed.

2.4. Aggregation of PM6 in Solution and Film

Having considered the optical and GIWAXS signatures of the acceptor materials, we now investigate the aggregation behavior of the electron donor material PM6. **Figure 7** shows the temperature-dependent evolution of the PL and absorption spectra of PM6 in oDCB at a concentration of 0.25 mg mL^{-1} upon cooling from 450 to 270 K. Here, PM6 follows the typical behavior of a conjugated polymer that aggregates upon cooling in solution. It displays an initial redshift upon cooling, followed by the appearance of a lower energy absorption, and a final sharpening of the vibrational structure at lower temperature, here 270 K. The PL intensity reduces as the aggregate absorption grows, which points toward a more H-like character.[47–48,50–51] Thus, PM6 undergoes a disorder–order transition with an onset temperature at T_{onset} = 420 K, i.e., well above room temperature. Above 420 K PM6 has only noninteracting chains. The PL spectrum is broad, which is typical for donor–acceptor polymers.[62–63] The spectral shape of the PL spectrum from the interacting chains corresponds to the spectra obtained at 270 K. For the absorption spectrum of the interacting chains, the contribution from the noninteracting chains needs to be subtracted (see the Supporting Information).[49,64] This implies that PM6 is one of the frequently used donor polymers that already contain aggregates in room temperature solution, a feature that has an impact on the resulting morphology in the thin film.[50–51] For applications such as solar cells, the amount of PM6 aggregates in room temperature solution can be modified through the usual parameters such as choice of solvent, temperature, molecular weight, polydispersity, and other approaches.[48,65–74]

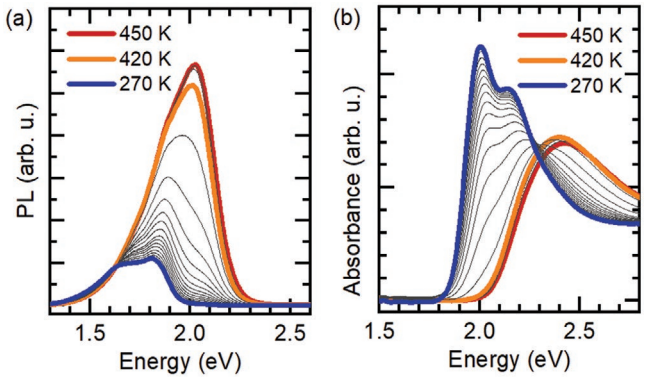

Figure 7. PL a) and absorption b) spectra of PM6 in oDCB at a concentration of 0.25 mg mL^{-1} upon cooling from 450 to 270 K in 10 K-steps. Spectra taken at characteristic temperatures are drawn with colored solid lines and given in the legend.

2.5. Blend Films

With the knowledge of the optical signatures of aggregates in Y6, N4, and PM6, we can now attempt to identify which species exist in blends of PM6:Y6 and PM6:N4. Solar cells made with such blends have previously been compared by Perdigón-Toro et al. They find a higher solar cell efficiency in the PM6:Y6 film, which is mainly a result of a higher open-circuit voltage V_{OC}. Perdigón-Toro et al. attributed this to a lower energetic disorder and higher phase purity in PM6:Y6. Temperature-dependent recombination studies revealed that free charge recombination is merely between a Gaussian-shaped highest occupied molecular orbital (HOMO) of the donor and a Gaussian-type lowest unoccupied molecular orbital (LUMO) density of states (DOS) of the acceptor in PM6:Y6, whereas recombination in PM6:N4 involves a wider Gaussian width of the acceptor LUMO and, in addition, an exponential tail in the HOMO DOS, causing a significant decrease of the resulting V_{OC}.[25]

In our work, we use blend films, prepared under the same conditions as Perdigón-Toro et al. and focus on the question how these blends differ regarding their content and nature of aggregated species. We use thermally annealed blend films with a material ratio of 1:1.2 for PM6:Y6 and 1:1.25 for PM6:N4 spun from chloroform with 0.5%/V CN as solvent additive. The absorption of the blend films is shown in **Figure 8**a. For both blend films, we observe two distinct absorption bands around 1.5 eV and around 2.0 eV, respectively, which are due to the absorption of the electron acceptor and the PM6, respectively. The absorption of N4 in the blend appears shifted to slightly higher energies compared to Y6. This suggests differences of the aggregation behavior between the acceptor compounds. The absorption of PM6 looks similar for both films, except for a slight difference in intensity, which may result from the slightly different material mixing ratios.

We can perform a spectral decomposition of the blend absorption by employing the parameters obtained from the Franck–Condon analysis of the neat films. It turns out that all values for the FC progression in Y6 and N4 are nearly identical in the blend and in the thermally annealed neat films (see the Supporting Information). For Y6, this is consistent with the results of molecular dynamics (MD) simulations, which show that the molecular packing of pristine Y6 is largely maintained in the blends.[7] Differences occur only in the oscillator strength of the aggregates' components and their contribution relative to the noninteracting chains. The fractional intensities of the different aggregate levels are shown in Figure 8b.

The most obvious difference in the PM6:Y6 film is a higher contribution of the J-like aggregates relative to the noninteracting chains, and a particularly strong contribution of *aggregate I* (red). This feature has much less intensity in the PM6:N4 film, which accounts for the apparent blueshift of the spectrum.

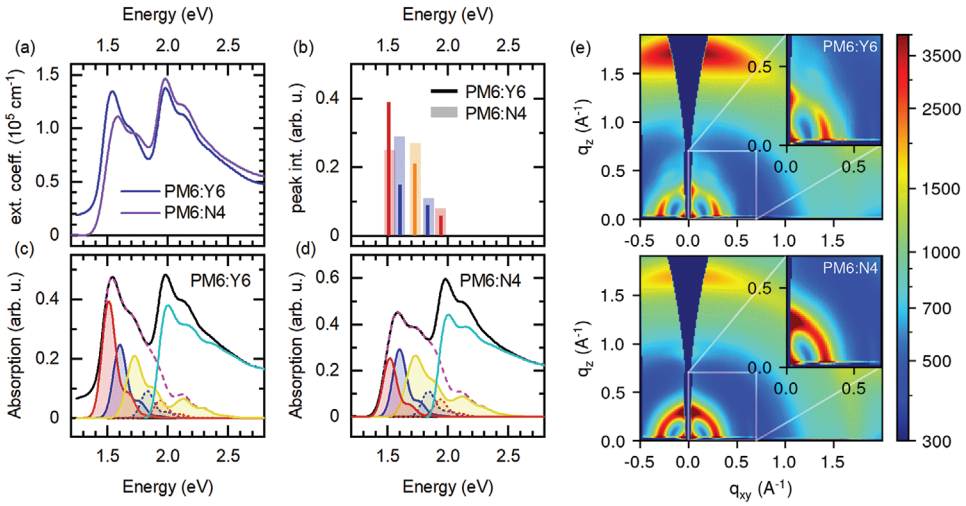

Figure 8. Absorption of TA blend films of a) PM6:Y6 (1:1.2) and PM6:N4 (1:1.25). b) Fractional intensities of the several phases of the acceptor compound in PM6:Y6 (solid line) and PM6:N4 (transparent bars) as obtained from the c,d) spectral decomposition of the absorption spectra of the blend films into a disordered phase of the acceptor compounds Y6 and N4 (dark yellow). The two acceptor aggregated phases (red, blue) with their low energy (solid line) and high energy (dotted line) progressions are shown respectively for N4 and Y6. The absorption contributed to PM6 is drawn with a turquoise line. e) 2D-GIWAXS images of PM6:Y6 (top) and PM6:N4 (bottom) measured on Si substrates. The inset shows a magnification of the low q-range (marked by the white square).

The higher degree of aggregation of Y6 in the blend film and the higher amount of *aggregate I* correlates to the better overall performance of the PM6:Y6 organic solar cell device than PM6:N4, which will be discussed below. The higher contribution of aggregates in the PM6:Y6 film is further consistent with GIWAXS measurements in the PM6:Y6 blend which show signatures of nanostructures arising from Y6 molecules, in contrast to the PM6:N4 film,[25], as illustrated by the GIWAXS data shown in Figure 8e. Several connected Y6 molecules are required to form such superstructures.

3. Discussion

In recent years, many studies focused on unveiling the structural and morphological properties of Y-type NFA materials and their impact on the photophysical properties when blended with electron donors, such as PM6. For example, X-ray scattering revealed that Y6 and some of its derivatives form a complex "honeycomb" structure in single crystals.[6–8,60,75] Molecular dynamics simulations show that pristine films of Y6 contain building blocks of this honeycomb structure, which are largely maintained when blended with PM6.[7,44] Extracted from these simulations, four dimer configurations have been identified with different orientations of the molecular core (C) and terminal (T), as illustrated in **Figure 9**.

We put our results in context with the structures reported by Kupgan et al.[44] For all samples in our study, we observe two aggregates, which differ in the interaction energy β and the distribution of the oscillator strength into the two levels. It is tempting to associate the dimers with the larger molecular overlap, i.e., CT–CT and CC–TT with the aggregates I that have a β just above 200 meV (c.f. Table 4), and the dimers with the smaller molecular overlap, such as TT and CT with aggregates II where β takes about half that value. The extent of the molecular overlap in the CC–TT arrangement appears to be similar to the one in the CT–CT configuration. By visual inspection, it is reasonable to expect the transition dipole moments for CC–TT to align in a parallel fashion thus yielding a predominant H-type character, whereas the more sequential alignment in CT–CT will result in a J-type nature. In this framework, the observed reorientation and change from H-like to J-like character of aggregate I during the thermal annealing of the N4 neat film would correspond to a reorientation from the CC–TT to the CT–CT configuration. In Y6, the formation of a CC–TT orientation seems to be inhibited by the closer position of the side-chain branching to the backbone and its associated steric demand, while it is enabled by the more remote branching point in N4. This conclusion also fits to the observed scattering pattern. Previous spectroscopic and molecular dynamics studies on other D–A-type molecules revealed that for banana shaped molecules, like the shape of the Y-family, there are different pathways for dimer formation that lead to structures with CT–CT or CC–TT character. Which pathway is accessible depends on the steric demand of the sidechains.[46,76]

The different branching point of the sidechain in N4 compared to Y6 can also account for the higher onset temperature of aggregate formation in MeTHF solution. Less steric hindrance of the sidechains enables electronic interaction of the backbones already at higher temperatures for N4, so that aggregation can occur. This is consistent with the observations by Lei et al. that moving the branching point away from a backbone results in stronger π-stacking interactions.[77] We consider that this higher onset temperature for aggregation is also the cause for the different orientation of the aggregates toward the substrate that we observe by GIWAXS measurements. We found an edge-on orientation for N4 and face-on for Y6, in accordance with earlier reports.[26] The higher onset temperature for aggregation, above room temperature, leads to the presence of aggregates already in solution prior to the film formation. Thereby, the π–π-interactions are already saturated to a certain degree, and the ability of the π-system to interact with the

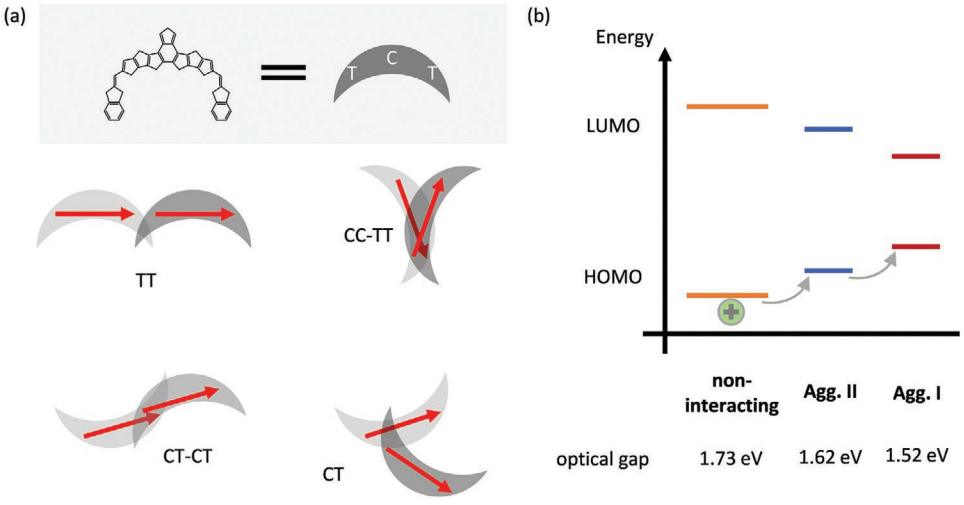

Figure 9. a) Schematic dimer configurations with interactions between the molecular core (C) and terminal (T) in different orientations as suggested by Kupgan et al. on the basis of MD simulations, along with our expected orientation of the transition dipole moments (red arrows). After.[44] b) Schematic illustrating possible positions of HOMO/LUMO levels of aggregate I and II in a qualitative manner.

substrate is reduced. Consequently, preferably the side chains interact with the substrate, leading to a predominant edge-on orientation. In contrast, Y6 with a clearly lower onset temperature (T_{onset} = 230 K) is well dissolved until shortly prior to the complete evaporation of the solvent. Thereby, the π-system of the molecules can interact with the substrate unimpededly, resulting in a face-on orientation.

By influencing the short-range order in neat films, we also expect the sidechains to have an influence on the solar cell performance of blends with PM6. Both PM6 blend films with Y6 and N4 are reported to show excellent power conversion efficiencies. However, the Y6 based devices exceed the performance of devices with N4.[25] Perdigón-Toro et al. attributed this to the unfavorable molecular edge-on orientation in the PM6:N4 blend, causing a reduced mobility. More importantly, the PM6:N4 blend was shown to exhibit a larger energetic disorder, in part with an exponential tail of trap states, which was shown to be the main reason for the smaller V_{OC} in PM6:N4 devices compared with PM6:Y6.[25–26]

We find that the absorption spectra of PM6:Y6 contain a higher fraction of interacting chromophores than PM6:N4, and among them a particularly dominant proportion of aggregate I. While we do not know the HOMO and LUMO levels for Aggregate I and Aggregate II relative to those of the noninteracting molecules, their lower optical gap suggests a concomitant HOMO destabilization and LUMO stabilization. Consequently, charges will predominantly relax toward interacting chromophores of Aggregate I. (c.f. Figure 9) From the results of Perdigón-Toro we conclude that the number and distribution of Aggregate I-type chromophores in PM6:Y6 is sufficient to support a good percolation path for the charge carriers. In contrast, either the fraction or the distribution (or both) of Aggregate I-type chromophores in the PM6:N4 blend is such that transport is disrupted, with Aggregate I-type chromophores providing trap states for electrons. We consider that the long-range Coulomb potential fluctuations due to the presence of trapped negative charges lead to an nearly exponential tail in the HOMO DOS.[54,78–79] We therefore conclude that the distribution of Aggregate I-type chromophores is responsible for the differences in the density of states (DOS) suggested by Perdigón-Toro et al., and the concomitant differences in solar cell performance.

We finally consider the effect of the different molecular packing in the two blends on the V_{OC}, which is found to be systematically lower in the PM6:N4 system.[25–26] It was shown that free charge recombination in PM6:Y6 proceeds almost entirely through the CT state[80] and we expect the same situation for the PM6:N4 blend. Then, the V_{OC} is determined by the energy, energetic disorder, and decay rate of the CT state.[81] Unfortunately, the CT state absorption and emission is nearly hidden under the strong NFA exciton in both systems;[25,80] therefore these properties are not attainable from optical spectroscopy. It has, however, been shown that the CT properties are largely linked to the energy, aggregation, and orientation of the molecules forming the CT states.[82] As we point out earlier, the most obvious difference in the optical spectra is a higher contribution of the J-like aggregates in the PM6:Y6 film compared to the noninteracting chains but also the PM6:N4 blend. In addition, the GIWAXS measurements in the PM6:Y6 blend show signatures of nanostructures arising from Y6 molecules, which require aggregates of several Y6 molecules to be present. Our GIWAXS results further reveal a more isotropic molecular orientation of the constituents in the PM6:N4 blend. In combination of these effects, we expect a larger energetic disorder of the CT state in the PM6:N4 blend, which will translate into a faster nonradiative decay and a smaller V_{OC}.[83]

4. Conclusion

In this study, we identify and analyze the intermolecular interactions in Y series NFAs, and the role of the side chain branching point in the formation of aggregates, in highly efficient blend systems by optical spectroscopy in combination with a Franck–Condon analysis. For this, we used the well-established Y-type acceptors Y6, with 2nd position branching of the alkyl side-chains, and N4 (4th position branching), and combine these with the donor polymer PM6. PM6 shows a distinct aggregate formation in films as well as in solution with an aggregate onset temperature well above the room temperature. The two acceptor molecules are found to form two aggregate types, though with clearly different nature. Y6 forms two J-like aggregates with different interaction energies, which can also be observed in blend films with PM6. In contrast, N4 forms aggregates with more H-like character as the further branching point of the side chains enables a more parallel stacking due to less steric hinderance. Upon thermal annealing or for longer storage time, this H-character converts into a J-like character, which can be traced back to a molecular reorientation, in accordance with GIWAXS measurements. In the thermally annealed blend films with PM6, the aggregates of both acceptor materials show similar character, though the proportions of the aggregates differ. The PM6:Y6 blend contains a significant higher amount of the acceptor aggregate with higher interaction energy. This dominant absorption of acceptor aggregate correlates with good transport properties and low energetic disorder in the corresponding solar cells.[25] This is not the case for the N4 phase in the PM6:N4 blend. There, an even distribution of the two types of aggregates and an overall lower contribution correlates with the appearance of an exponential tail in the DOS of the PM6 HOMO, consistent with the classical picture of DOS broadening by counter-charges on trapped isolated lower energy sites. In this way, the modification of the aggregation behavior through the slight extension of the side chain in the acceptor N4 causes a substantial change in the electronic structure of the donor PM6, with strong impact on the solar cell performance.

5. Experimental Section

The electron acceptor Y6 and the donor polymer PM6 were purchased by "1-material." N4 was synthesized as described.[26] For temperature-dependent solution measurements, N4 and Y6 at 0.15 mg mL^{-1} in MeTHF were dissolved. This corresponds to a molar concentration of about 1×10^{-4} mol L^{-1} for both materials. PM6 was dissolved in ortho-dichlorobenzene (ODB) at a concentration of 0.25 mg mL^{-1}. The solutions were stirred for at least 1 h at 50 °C to ensure complete dissolution of the materials. Temperature-dependent absorption and

emission measurements were carried out using a home-built setup. The solutions were filled in a 1 mm fused silica cuvette and placed in a temperature controlled continuous flow helium cryostat by Oxford Instruments. After reaching each temperature step of the measurement, waited for 15 min to ensure a fully equilibrated system before taking the measurement. The lowest accessible temperature was determined by the glass transition temperature of MeTHF, i.e., 137 K. A tungsten lamp is used as light source for absorption measurements. For emission measurements, a 405 nm continuous wave diode laser from Coherent was used to excite the PM6 samples and a 659 nm continuous wave diode laser for the Y6 and N4 samples. A spectrograph Andor Shamrock SR303i coupled to a CCD camera (Andor iDus 420) functions as detection system.

For neat film samples, solutions of neat Y6 and of neat N4 in chloroform at 12 mg mL^{-1}, and of neat PM6 in chlorobenzene at 8 mg mL^{-1} were prepared. Solutions of blends with PM6:Y6 in weight ratios of 1:1.2, and of PM6:N4 (weight ratio 1:1.25) were prepared in chloroform at a total concentration of 16 mg mL^{-1}. All solutions were mixed with 0.5% chloronaphthalene (CN) and then stirred for at least 2 h at 50 °C. All films were prepared by spin-casting the solution in a glovebox with nitrogen atmosphere at room temperature with 1000 rpm. Thermal annealing (TA) was conducted at 90 °C for 5 min. UV–vis absorption spectra of films at room temperature were captured with a Cary 5000 UV–vis spectrometer.

GIWAXS on neat films coated on silicon substrates was performed in vacuum at RT on a laboratory system at the University of Bayreuth (Xeuss 3.0, Xenocs SAS, Grenoble, France) with a Cu Kα source (λ = 1.54 Å), a Dectris EIGER 2R 1 M detector, and a sample-to-detector distance of 52.5 mm. Scattering experiments were carried out on silicon substrates due to decreased scattering background compared to glass. Figure S9 (Supporting Information) shows the GIWAXS data on glass for comparison. The presented *q*-profiles are cake cuts covering an azimuthal angle of 70°–110° for the cuts in the vertical direction and 0°–20° as well as 160°–180° for the cuts in the horizontal direction. The 2D GIWAXS measurements on blend films were performed on PEDOT:PSS (poly(3,4-ethylenedioxythiophene) polystyrene sulfonate) coated silicon substrates in vacuum at RT at the Soft Matter Interfaces beamline (12-ID) at the National Synchrotron Lightsource II (NSLS-II) at Brookhaven National Laboratory (λ = 0.77 Å), with a Dectris Pilatus200KW detector with a sample-to-detector distance of 275 mm at different rotational angles. These measurements are averages over 6 positions on the sample each measured for 20 s to reduce effects due to inhomogeneities. Changes in intensity profiles with time were tested and no beam damage was determined for 20 s of exposure.

Supporting Information

Supporting Information is available from the Wiley Online Library or from the author.

Acknowledgements

E.M.H. and F.E. acknowledge funding from SolarEraNet (No. NFA4R2ROPV) and the DFG (INST 91/443-1). F.E. thanks the Elite Study Program Macromolecular Science within the Elite Network of Bavaria (ENB) for support. This research used the Soft Matter Interfaces Beamline (SMI, Beamline 12-ID) of the National Synchrotron Light Source II, a US Department of Energy (DOE) Office of Science User Facility operated for the DOE Office of Science by Brookhaven National Laboratory under Contract No. DE-SC0012704. L.P.T. and D.N. acknowledge financial support by the DFG HIOS (Project No. 182087777 – SFB 951). A.K. and D.K. thank the Bayerisches Staatsministerum für Wissenschaft und Kunst for funding in the framework of the "SolTechGoHybrid" initiative.

Open access funding enabled and organized by Projekt DEAL.

Conflict of Interest

The authors declare no conflict of interest.

Data Availability Statement

The data that support the findings of this study are available from the corresponding author upon reasonable request.

Keywords

charge-transfer states, Frank–Condon analysis, morphology, organic solar cells

Received: May 19, 2022
Revised: July 1, 2022
Published online: August 23, 2022

[1] L. Liu, S. Chen, Y. Qu, X. Gao, L. Han, Z. Lin, L. Yang, W. Wang, N. Zheng, Y. Liang, Y. Tan, H. Xia, F. He, *Adv. Mater.* **2021**, *33*, 2101279.
[2] J. Yuan, Y. Zhang, L. Zhou, G. Zhang, H.-L. Yip, T.-K. Lau, X. Lu, C. Zhu, H. Peng, P. A. Johnson, M. Leclerc, Y. Cao, J. Ulanski, Y. F. Li, Y. Zou, *Joule* **2019**, *3*, 1140.
[3] F. Liu, L. Zhou, W. Liu, Z. Zhou, Q. Yue, W. Zheng, R. Sun, W. Liu, S. Xu, H. Fan, L. Feng, Y. Yi, W. Zhang, X. Zhu, *Adv. Mater.* **2021**, *33*, 2100830.
[4] L. Zhan, S. Li, T.-K. Lau, Y. Cui, X. Lu, M. Shi, C.-Z. Li, H. Li, J. Hou, H. Chen, *Energy Environ. Sci.* **2020**, *13*, 635.
[5] J. Yuan, H. Zhang, R. Zhang, Y. Wang, J. Hou, M. Leclerc, X. Zhan, F. Huang, F. Gao, Y. Zou, Y. Li, *Chem* **2020**, *6*, 2147.
[6] L. Zhu, M. Zhang, G. Q. Zhou, T. Y. Hao, J. Q. Xu, J. Wang, C. Q. Qiu, N. Prine, J. Ali, W. Feng, X. D. Gu, Z. F. Ma, Z. Tang, H. M. Zhu, L. Ying, Y. M. Zhang, F. Liu, *Adv. Energy Mater.* **2020**, *10*, 1904234.
[7] G. C. Zhang, X. K. Chen, J. Y. Xiao, P. C. Y. Chow, M. R. Ren, G. Kupgan, X. C. Jiao, C. C. S. Chan, X. Y. Du, R. X. Xia, Z. M. Chen, J. Yuan, Y. Q. Zhang, S. F. Zhang, Y. D. Liu, Y. P. Zou, H. Yan, K. S. Wong, V. Coropceanu, N. Li, C. J. Brabec, J. L. Bredas, H. L. Yip, Y. Cao, *Nat. Commun.* **2020**, *11*, 3943.
[8] W. G. Zhu, A. P. Spencer, S. Mukherjee, J. M. Alzola, V. K. Sangwan, S. H. Amsterdam, S. M. Swick, L. O. Jones, M. C. Heiber, A. A. Herzing, G. P. Li, C. L. Stern, D. M. DeLongchamp, K. L. Kohlstedt, M. C. Hersam, G. C. Schatz, M. R. Wasielewski, L. X. Chen, A. Facchetti, T. J. Marks, *J. Am. Chem. Soc.* **2020**, *142*, 14532.
[9] R. J. Ma, Y. Tao, Y. Z. Chen, T. Liu, Z. H. Luo, Y. Guo, Y. Q. Xiao, J. Fang, G. Y. Zhang, X. J. Li, X. Guo, Y. P. Yi, M. J. Zhang, X. H. Lu, Y. F. Li, H. Yan, *Sci. China: Chem.* **2021**, *64*, 581.
[10] S. Bao, H. Yang, H. Fan, J. Zhang, Z. Wei, C. Cui, Y. Li, *Adv. Mater.* **2021**, *33*, 2105301.
[11] J. Gao, X. Ma, C. Xu, X. Wang, J. H. Son, S. Y. Jeong, Y. Zhang, C. Zhang, K. Wang, L. Niu, J. Zhang, H. Y. Woo, J. Zhang, F. Zhang, *Chem. Eng. J.* **2022**, *428*, 129276.
[12] Y. Cui, Y. Xu, H. Yao, P. Bi, L. Hong, J. Zhang, Y. Zu, T. Zhang, J. Qin, J. Ren, *Adv. Mater.* **2021**, *33*, 2102420.
[13] K. Chong, X. Xu, H. Meng, J. Xue, L. Yu, W. Ma, Q. Peng, *Adv. Mater.* **2022**, *34*, 2109516.
[14] Z. Zheng, J. Wang, P. Bi, J. Ren, Y. Wang, Y. Yang, X. Liu, S. Zhang, J. Hou, *Joule* **2021**, *6*, 171.

[15] A. Armin, W. Li, O. J. Sandberg, Z. Xiao, L. M. Ding, J. Nelson, D. Neher, K. Vandewal, S. Shoaee, T. Wang, H. Ade, T. Heumuller, C. Brabec, P. Meredith, *Adv. Energy Mater.* **2021**, *11*, 2003570.
[16] C. Yan, S. Barlow, Z. Wang, H. Yan, A. K.-Y. Jen, S. R. Marder, X. Zhan, *Nat. Rev. Mater.* **2018**, *3*, 18003.
[17] J. Zhang, H. S. Tan, X. Guo, A. Facchetti, H. Yan, *Nat. Energy* **2018**, *3*, 720.
[18] Q. Yue, W. Liu, X. Zhu, *J. Am. Chem. Soc.* **2020**, *142*, 11613.
[19] W. Liu, X. Xu, J. Yuan, M. Leclerc, Y. Zou, Y. Li, *ACS Energy Lett.* **2021**, *6*, 598.
[20] T. Zhang, C. An, P. Bi, Q. Lv, J. Qin, L. Hong, Y. Cui, S. Zhang, J. Hou, *Adv. Energy Mater.* **2021**, *11*, 2101705.
[21] R. J. Ma, T. Liu, Z. H. Luo, K. Gao, K. Chen, G. Y. Zhang, W. Gao, Y. Q. Xiao, T. K. Lau, Q. P. Fan, Y. Z. Chen, L. K. Ma, H. L. Sun, G. L. Cai, T. Yang, X. H. Lu, E. G. Wang, C. L. Yang, A. K. Y. Jen, H. Yan, *ACS Energy Lett.* **2020**, *5*, 2711.
[22] Z. H. Luo, R. J. Ma, T. Liu, J. W. Yu, Y. Q. Xiao, R. Sun, G. S. Xie, J. Yuan, Y. Z. Chen, K. Chen, G. D. Chai, H. L. Sun, J. Min, J. Zhang, Y. P. Zou, C. L. Yang, X. H. Lu, F. Gao, H. Yan, *Joule* **2020**, *4*, 1236.
[23] G. D. Chai, Y. Chang, J. Q. Zhang, X. P. Xu, L. Y. Yu, X. H. Zou, X. J. Li, Y. Z. Chen, S. W. Luo, B. B. Liu, F. J. Bai, Z. H. Luo, H. Yu, J. E. Liang, T. Liu, K. S. Wong, H. Zhou, Q. Peng, H. Yan, *Energy Environ. Sci.* **2021**, *14*, 3469.
[24] L. Zhu, M. Zhang, J. Xu, C. Li, J. Yan, G. Zhou, W. Zhong, T. Hao, J. Song, X. Xue, Z. Zhou, R. Zeng, H. Zhu, C.-C. Chen, R. C. I. MacKenzie, Y. Zou, J. Nelson, Y. Zhang, Y. Sun, F. Liu, *Nat. Mater.* **2022**, *21*, 656.
[25] L. Perdigón-Toro, L. Q. Phuong, F. Eller, G. Freychet, E. Saglamkaya, J. I. Khan, Q. Wei, S. Zeiske, D. Kroh, S. Wedler, A. Köhler, A. Armin, F. Laquai, E. M. Herzig, Y. Zou, S. Shoaee, D. Neher, *Adv. Energy Mater.* **2022**, *12*, 2103422.
[26] K. Jiang, Q. Wei, J. Y. L. Lai, Z. Peng, H. K. Kim, J. Yuan, L. Ye, H. Ade, Y. Zou, H. Yan, *Joule* **2019**, *3*, 3020.
[27] G. Yao, Y. Ge, X. Xiao, L. Zhang, N. Yi, H. Luo, S. Yuan, W. Zhou, *ACS Appl. Energy Mater.* **2022**, *5*, 1193.
[28] S. Li, C.-Z. Li, M. Shi, H. Chen, *ACS Energy Lett.* **2020**, *5*, 1554.
[29] S. Dong, T. Jia, K. Zhang, J. Jing, F. Huang, *Joule* **2020**, *4*, 2004.
[30] Y. Qin, Y. Xu, Z. Peng, J. Hou, H. Ade, *Adv. Funct. Mater.* **2020**, *30*, 2005011.
[31] X. J. Li, H. Huang, I. Angunawela, J. D. Zhou, J. Q. Du, A. Liebman-Pelaez, C. H. Zhu, Z. J. Zhang, L. Meng, Z. Q. Xie, H. Ade, Y. F. Li, *Adv. Funct. Mater.* **2020**, *30*, 1906855.
[32] J. Q. Zhang, F. J. Bai, I. Angunawela, X. Y. Xu, S. W. Luo, C. Li, G. D. Chai, H. Yu, Y. Z. Chen, H. W. Hu, Z. F. Ma, H. Ade, H. Yan, *Adv. Energy Mater.* **2021**, *11*, 2102596.
[33] Z. H. Luo, R. J. Ma, Z. X. Chen, Y. Q. Xiao, G. Y. Zhang, T. Liu, R. Sun, Q. Zhan, Y. Zou, C. Zhong, Y. Z. Chen, H. L. Sun, G. D. Chai, K. Chen, X. G. Guo, J. Min, X. H. Lu, C. L. Yang, H. Yan, *Adv. Energy Mater.* **2020**, *10*, 2002649.
[34] Z. Luo, R. Sun, C. Zhong, T. Liu, G. Zhang, Y. Zou, X. Jiao, J. Min, C. Yang, *Sci. China: Chem.* **2020**, *63*, 361.
[35] Z.-F. Yao, J.-Y. Wang, J. Pei, *Cryst. Growth Des.* **2018**, *18*, 7.
[36] L. Hong, H. F. Yao, Z. Wu, Y. Cui, T. Zhang, Y. Xu, R. N. Yu, Q. Liao, B. W. Gao, K. H. Xian, H. Y. Woo, Z. Y. Ge, J. H. Hou, *Adv. Mater.* **2019**, *31*, 1903441.
[37] D. Mo, H. Chen, Y. Zhu, H.-H. Huang, P. Chao, F. He, *ACS Appl. Mater. Interfaces* **2020**, *12*, 28329.
[38] Y. Guo, G. Han, Y. Yi, *J. Energy Chem.* **2019**, *35*, 138.
[39] T. Yasuda, K. Sakamoto, *Org. Electron.* **2018**, *62*, 429.
[40] C. Yan, Y. Wu, J. Wang, R. Li, P. Cheng, H. Bai, Z. Zhan, W. Ma, X. Zhan, *Dyes Pigm.* **2017**, *139*, 627.
[41] S. Athanasopoulos, H. Bässler, A. Köhler, *J. Phys. Chem. Lett.* **2019**, *10*, 7107.
[42] S. N. Hood, I. Kassal, *J. Phys. Chem. Lett.* **2016**, *7*, 4495.
[43] M. Schubert, D. Dolfen, J. Frisch, S. Roland, R. Steyrleuthner, B. Stiller, Z. Chen, U. Scherf, N. Koch, A. Facchetti, D. Neher, *Adv. Energy Mater.* **2012**, *2*, 369.
[44] G. Kupgan, X.-K. Chen, J.-L. Brédas, *Mater. Today Adv.* **2021**, *11*, 100154.
[45] Y. Liu, J. Zhao, Z. Li, C. Mu, W. Ma, H. Hu, K. Jiang, H. Lin, H. Ade, H. Yan, *Nat. Commun.* **2014**, *5*, 5293.
[46] S. Wedler, A. Bourdick, S. Athanasopoulos, S. Gekle, F. Panzer, C. McDowell, T.-Q. Nguyen, G. C. Bazan, A. Köhler, *J. Mater. Chem. C* **2020**, *8*, 4944.
[47] F. Panzer, H. Bässler, A. Köhler, *J. Phys. Chem. Lett.* **2017**, *8*, 114.
[48] F. Panzer, H. Bässler, R. Lohwasser, M. Thelakkat, A. Köhler, *J. Phys. Chem. Lett.* **2014**, *5*, 2742.
[49] F. Panzer, M. Sommer, H. Bässler, M. Thelakkat, A. Köhler, *Macromolecules* **2015**, *48*, 1543.
[50] M. Reichenberger, D. Kroh, G. M. Matrone, K. Schötz, S. Pröller, O. Filonik, M. E. Thordardottir, E. M. Herzig, H. Bässler, N. Stingelin, A. Köhler, *J. Polym. Sci. B: Polym. Phys.* **2018**, *56*, 532.
[51] C. Scharsich, F. S. Fischer, K. Wilma, R. Hildner, S. Ludwigs, A. Köhler, *J. Polym. Sci. B: Polym. Phys.* **2015**, *53*, 1416.
[52] A. Köhler, S. T. Hoffmann, H. Bässler, *J. Am. Chem. Soc.* **2012**, *134*, 11594.
[53] F. C. Spano, *Acc. Chem. Res.* **2010**, *43*, 429.
[54] A. Köhler, H. Bässler, *Electronic Processes in Organic Semiconductors: An Introduction*, John Wiley & Sons, New York **2015**.
[55] K. Cai, J. Xie, D. Zhang, W. Shi, Q. Yan, D. Zhao, *J. Am. Chem. Soc.* **2018**, *140*, 5764.
[56] M. Reichenberger, D. Kroh, G. M. Matrone, K. Schötz, S. Pröller, O. Filonik, M. E. Thordardottir, E. M. Herzig, H. Bässler, N. Stingelin, *J. Polym. Sci. B: Polym. Phys.* **2018**, *56*, 532.
[57] M. Kasha, *Radiat. Res.* **1963**, *20*, 55.
[58] M. Kasha, H. R. Rawls, M. A. El-Bayoumi, *Pure Appl. Chem.* **1965**, *11*, 371.
[59] J. Gao, J. Wang, Q. An, X. Ma, Z. Hu, C. Xu, X. Zhang, F. Zhang, *Sci. China Chem.* **2020**, *63*, 83.
[60] F. Lin, K. Jiang, W. Kaminsky, Z. Zhu, A. K.-Y. Jen, *J. Am. Chem. Soc.* **2020**, *142*, 15246.
[61] Z. Bi, K. Chen, L. Gou, Y. Guo, X. Zhou, H. B. Naveed, J. Wang, Q. Zhu, J. Yuan, C. Zhao, K. Zhou, S. Chandrabose, Z. Tang, Y. Yi, J. M. Hodgkiss, L. Zhang, W. Ma, *J. Mater. Chem. A* **2021**, *9*, 16733.
[62] L. Lin, Y. Morisaki, Y. Chujo, *Int. J. Polym. Sci.* **2010**, 2010.
[63] F. B. Dias, S. Pollock, G. Hedley, L.-O. Pålsson, A. Monkman, I. I. Perepichka, I. F. Perepichka, M. Tavasli, M. R. Bryce, *J. Phys. Chem. B* **2006**, *110*, 19329.
[64] M. Reichenberger, S. Baderschneider, D. Kroh, S. Grauf, J. r. Köhler, R. Hildner, A. Köhler, *Macromolecules* **2016**, *49*, 6420.
[65] Q. Liu, J. Fang, J. Wu, L. Zhu, X. Guo, F. Liu, M. Zhang, *Chin. J. Chem.* **2021**, *39*, 1941.
[66] C. H. Guo, D. H. Li, L. Wang, B. C. Du, Z. X. Liu, Z. Q. Shen, P. Wang, X. Zhang, J. L. Cai, S. L. Cheng, C. Yu, H. Wang, D. Liu, C. Z. Li, T. Wang, *Adv. Energy Mater.* **2021**, *11*, 2102000.
[67] D. Li, X. Chen, J. Cai, W. Li, M. Chen, Y. Mao, B. Du, J. A. Smith, R. C. Kilbride, M. E. O'Kane, X. Zhang, Y. Zhuang, P. Wang, H. Wang, D. Liu, R. A. L. Jones, D. G. Lidzey, T. Wang, *Sci. China Chem.* **2020**, *63*, 1461.
[68] B. Du, R. Geng, W. Tan, Y. Mao, D. Li, X. Zhang, D. Liu, W. Tang, W. Huang, T. Wang, *J. Energy Chem.* **2021**, *54*, 131.
[69] L. Zhan, S. Li, X. Xia, Y. Li, X. Lu, L. Zuo, M. Shi, H. Chen, *Adv. Mater.* **2021**, *33*, 2007231.
[70] Y. P. Xie, Y. H. Cai, L. Zhu, R. X. Xia, L. L. Ye, X. Feng, H. L. Yip, F. Liu, G. H. Lu, S. T. Tan, Y. M. Sun, *Adv. Funct. Mater.* **2020**, *30*, 2002181.
[71] T. Shan, Y. Zhang, Y. Wang, Z. Xie, Q. Wei, J. Xu, M. Zhang, C. Wang, Q. Bao, X. Wang, C. Chen, J. Huang, Q. Chen, F. Liu, L. Chen, H. Zhong, *Nat. Commun.* **2020**, *11*, 5585.

[72] H. Fu, W. Gao, Y. Li, F. Lin, X. Wu, J. H. Son, J. Luo, H. Y. Woo, Z. Zhu, A. K. Y. Jen, *Small Methods* **2020**, *4*, 2000687.
[73] Y. Wei, J. Yu, L. Qin, H. Chen, X. Wu, Z. Wei, X. Zhang, Z. Xiao, L. Ding, F. Gao, H. Huang, *Energy Environ. Sci.* **2021**, *14*, 2314.
[74] L. Arunagiri, G. Zhang, H. Hu, H. Yao, K. Zhang, Y. Li, P. C. Chow, H. Ade, H. Yan, *Adv. Funct. Mater.* **2019**, *29*, 1902478.
[75] C. Xiao, C. Li, F. Liu, L. Zhang, W. Li, *J. Mater. Chem. C* **2020**, *8*, 5370.
[76] A. Bourdick, M. Reichenberger, A. Stradomska, G. C. Bazan, T.-Q. Nguyen, A. Köhler, S. Gekle, *J. Phys. Chem. B* **2018**, *122*, 9191.
[77] T. Lei, J. H. Dou, J. Pei, *Adv. Mater.* **2012**, *24*, 6457.
[78] V. Arkhipov, P. Heremans, E. Emelianova, H. Baessler, *Phys. Rev. B* **2005**, *71*, 045214.
[79] I. Hulea, H. Brom, A. Houtepen, D. Vanmaekelbergh, J. Kelly, E. Meulenkamp, *Phys. Rev. Lett.* **2004**, *93*, 166601.
[80] L. Perdigon-Toro, L. Q. Phuong, S. Zeiske, K. Vandewal, A. Armin, S. Shoaee, D. Neher, *ACS Energy Lett.* **2021**, *6*, 557.
[81] T. M. Burke, S. Sweetnam, K. Vandewal, M. D. McGehee, *Adv. Energy Mater.* **2015**, *5*, 1500123.
[82] X. K. Chen, M. K. Ravva, H. Li, S. M. Ryno, J. L. Brédas, *Adv. Energy Mater.* **2016**, *6*, 1601325.
[83] Z. Zheng, N. R. Tummala, T. Wang, V. Coropceanu, J. L. Brédas, *Adv. Energy Mater.* **2019**, *9*, 1803926.